



# Waste plastic derived carbon supported Mo<sub>2</sub>C composite catalysts for hydrogen production and energy storage applications

Rameez Ahmad Mir, O.P. Pandey\*

Functional Materials Lab, SPMS, TIET, Patiala (Pb), India

## ARTICLE INFO

### Article history:

Received 16 July 2018

Received in revised form

20 November 2018

Accepted 1 February 2019

Available online 5 February 2019

### Keywords:

Hydrogen evolution reaction

Carbon coating

Plastic waste

Carburization

Double layer capacitance

## ABSTRACT

The valuable approach to produce hydrogen as fuel for efficient and clean energy source is electrochemical water splitting. Synthesis of efficient and economic catalysts for hydrogen evolution reaction (HER) is necessary for commercial scale production of hydrogen. The essential and successive path in the field of energy transformation and capacitors are the synthesis of the high performance electrodes. Herein, we report the synthesis of molybdenum carbide (MoC/Mo<sub>2</sub>C) via in-situ carburization route. The work reports utilization of waste plastics for the synthesis of molybdenum carbide carbon nanocomposites, which are subsequently used for the hydrogen production and energy storage applications. The environmental issues caused by the waste plastics and the limitations of recycling/reuse has been addressed. The effect of carburization temperature, the role of the initial amount of carbon on phase formation of molybdenum carbide and electrochemical activities has been discussed. The XRD results confirm the pure phase formation of Mo<sub>2</sub>C at 700 and 800 °C. The adherent nature of residual carbon determined by Raman spectroscopy and HRTEM analysis in the synthesized powders affect the electrochemical properties, hydrogen evolution reaction (HER), electric double layer capacitance (EDLC) as well as electrochemical impedance spectroscopy (EIS). The amount of adherent residual surface carbon determined by TGA analysis plays imperative role in protecting the carbide particles from oxidation and firmly contributes to the electrochemical activity. The synthesized material shows the higher stability up to 2000 cyclic voltammetry (CV) cycles in the voltage range 0.2 to −0.3 V. The powders synthesized at higher temperature shows the higher double layer capacitance ( $C_{dl}$ ) and specific capacitance to the tune of 19.46 mFcm<sup>−2</sup> and 55.6 Fg<sup>−1</sup>, respectively. The graphitic carbon coating obtained at relatively higher temperature affects the storage capacity/retention as well as the charge transfer resistance.

© 2019 Elsevier Ltd. All rights reserved.

## 1. Introduction

Hydrogen is contemplated as the efficient, sustainable and zero carbon emission energy source. The most suitable promising energy substitution to diminishing fossil fuels is hydrogen (Li et al., 2016; Shi et al., 2017). However, hydrogen production is still challenging problem in the present era. One of the irresistible methods for producing hydrogen (H<sub>2</sub>) by hydrogen evolution reaction (HER) through electrochemical water splitting is indispensable owing to its high efficiency (Liao et al., 2014; Mu et al., 2016; Qiao et al., 2015; Yang et al., 2016). Presently the key issue of this method is the requirement of the highly active electrocatalyst to promote HER performance. Till date, platinum (Pt.) is considered as the suitable

and efficient electrocatalyst for HER, but its practical use is limited due to its higher cost and low profusion (Yang et al., 2016; Youn et al., 2014).

The state of art to develop economic and noble-metal free electrocatalysts for HER having high activity/efficiency, long term stability and high elemental abundance in nature is the need of present era (McKone et al., 2014). In the forefront, efforts are made to use the transition metals and their phosphides, nitrides, chalcogenides and carbides, as the promising non-noble metal free catalysts for HER (Chen et al., 2014; Christensen, 2016; Hu et al., 2010; Ojha et al., 2017). Molybdenum carbide (Mo<sub>2</sub>C/MoC) an interesting candidate among transition metal carbides (TMCs) has attained special level as catalyst due to variation in its electronic features, which resembles to Pt (Wan et al., 2014; Wu et al., 2015). The commercial grade micron-sized molybdenum carbides have not shown better efficiency for all the practical purposes. However, the HER activity of Mo<sub>2</sub>C gets enhanced when synthesized in

\* Corresponding author.

E-mail address: [oppandey@thapar.edu](mailto:oppandey@thapar.edu) (O.P. Pandey).

nanoscale with different morphological structures. To achieve high surface area for electrocatalytic activity, the surface carbide carbon plays a vital role (Tang et al., 2016). The crystallite size, morphology and nature of carbon coating encapsulating the carbide particles depend on synthesis method/parameters and amount of carbon source (Mo et al., 2015). Different synthesis methods have been adopted to synthesize nanostructured Mo<sub>2</sub>C with more active sites (Huang et al., 2016; Liao et al., 2014; Michalsky et al., 2014; Vrabel and Hu, 2012; Wu et al., 2015; Xiao et al., 2014) and composites of supported carbon matrix in different forms to improve HER activity (Li et al., 2016; Pang et al., 2010; Shi et al., 2016; Sljukic et al., 2015; Yang et al., 2016; Zhang et al., 2015). Carbon support on Mo<sub>2</sub>C in different forms also enhances the charge storage capacity of the nano-composites in supercapacitors and EDLCs (Leis and Perkson, 2010; Li et al., 2016).

The key parameter of the present work is the utilization of laboratory waste plastics as the source of carbon for the synthesis of carbon supported molybdenum carbides in an autoclave. The throw away habit of waste plastics has created lot of environmental problems and threat to water bodies. In order to overcome this problem, various thermochemical recycling processes viz thermo-catalytic, pyrolysis, incineration, gasification, pyrolysis-reforming strategies have been adopted to convert waste plastics into transport fuel grade hydrocarbons (Begum et al., 2012; Ohnishi et al., 2018; Ramos et al., 2018; Zhang et al., 2017). The type of thermochemical process selected for converting waste plastics into usable energy depends on the feed stock availability and efficiency of conversion (Begum et al., 2012). All the above processes are multistep and require special type of reactors to overcome the issues of toxic gas emissions in pyrolysis/incineration. The bio-oil thus obtained is further processed to obtain plastic waste derived gasoline, diesel and other petro products as is being done in different refineries. Further processing under different conditions using different catalysts is done to enhance the efficiency of the obtained bio-oil (Hazrat et al., 2014). Barbarias et al. (Barbarias et al., 2018) have shown the significant increase in H<sub>2</sub> production from different waste plastic polymers by pyrolysis and inline steam reforming process. The strong dependence of pyrolysis process on product characteristics and plastic composition restricted its large scale use. However, this limitation has been overcome by gasification process (Anuar Sharuddin et al., 2016; Lopez et al., 2018). Miskolczi et al. (Miskolczi et al., 2009) used thermo-catalytic process for the transformation of polypropylene based plastic wastes into gasoline and light oil. Recently the generation of H<sub>2</sub> and carbon nano tubes (CNTs) from waste plastics have been reported, where the role of metal catalyst used during processing has been highlighted (Yao et al., 2018). To increase the efficiency of the H<sub>2</sub> production from waste plastics the search of suitable and stable catalyst is still prevailing. The CNTs are the useful catalyst and catalyst support materials in various energy production and storage devices. However, the zero emission of the toxic gases in the thermo chemical conversion of plastic wastes to fuel is still an unresolved and critical issue.

In order to address above issues, the present work is undertaken to synthesize Mo<sub>2</sub>C in an autoclave from these waste plastics for energy production and storage. The carbonaceous gases produced by waste plastics inside the autoclave helps in reduction of MoO<sub>3</sub> and carburize to Mo<sub>x</sub>C (x = 1,2). The current demonstrated process is environment friendly, inexpensive and easy to scale up.

In this report carburization temperature and amount of initial carbon has been varied to obtain single phase Mo<sub>2</sub>C with different morphological features. Herein, the influence of residual carbon content and nature of carbon for HER activity and charge storage capacity over Mo<sub>2</sub>C has been studied. The synthesized products

MoC/Mo<sub>2</sub>C incorporated in the carbon matrix exhibits superior stability and enhanced HER performance than the supported non-precious metal and bulk materials in the acidic medium (Zou and Zhang, 2015). The EDLC measurements of high temperature synthesized Mo<sub>2</sub>C particles with graphitic carbon support have shown improved storage efficiency (Li et al., 2016). The present work demonstrates the significance of amount carbon for synthesis of pure phase Mo<sub>2</sub>C electrocatalyst, HER performance and the charge storage capacity. The present facile method is the promising approach to synthesize low cost noble-metal free electrocatalysts for the water splitting.

## 2. Materials and methods

### 2.1. Synthesis

For the synthesis of (MoC/Mo<sub>2</sub>C), molybdenum trioxide (MoO<sub>3</sub>) was taken as molybdenum precursor. To facilitate its reduction magnesium (Mg) was added in it. Both the compounds were mixed properly in agate mortar. The laboratory plastic waste pipette tip was used for the first time for the synthesis of Mo<sub>2</sub>C. The pipette was washed properly with water, cut into small pieces and dried in vacuum oven at 40 °C. The mixed mixture of (MoO<sub>3</sub> + Mg) and Xg (X = 0.25, 0.5, 0.75, 1) of plastic waste was put in an autoclave and sealed properly. The autoclave was placed inside the resistance heating furnace as shown in Fig. S1 (Supplementary Information, SI). Its temperature was raised slowly to the required temperature. The obtained powder was further processed as reported elsewhere and shown in Fig. S1, (SI) (Mir et al., 2017). To study the influence of initial carbon content on carbide phase formation, the amount of initial carbon was varied. The details of the synthesis parameters and the sample labels are given in Table 1.

### 2.2. Characterization

The synthesized powders so obtained were characterized for phase formation and structural analysis by X-ray diffraction (XRD) PANalytical X-Pert-Pro having  $\lambda = 1.5406 \text{ \AA}$  (CuK $\alpha$ ). The X-ray diffraction pattern was measured from 20°–80° in a step of 0.013°. The phase confirmation of the product powders was done using X-Pert High Score Plus (ICDD data base). The morphological and microstructural studies of carbon supported Mo<sub>2</sub>C nano powders were done by field- emission scanning electron microscope (FE-SEM) (Hitachi SU 8010) at 15 kV and transmission electron microscope (TEM) (JEOL 2100 F) at 200 kV. The presence of different elements in the synthesized samples was checked by energy dispersive spectra (EDS). To know the surface chemical composition of elements and their valence states, X-ray photoelectron spectroscopy (XPS) was done by XPS spectrometer (ESCA+) using 1486.7 eV (Al-K $\alpha$  radiation) source functioning at 15 kV and 15 mA. Raman spectroscopy using STR 500 Airix was done to determine the degree of graphitization. TG (NETZSCH STA 449F3) was done in air atmosphere at a heating rate of 5 °C/min. Nitrogen sorption surface analysis was done to estimate the surface area, size of pore and its volume by Micro Trac Bell mini-II.

### 2.3. Electrochemical activity

The electrochemical studies of the synthesized samples were done by three electrode cell assembly of the SP300 (Bio-logic EC Lab) instrument as given in Fig. S1, (SI). To prepare the working electrode, the procedure as reported in literature with variation in voltage range was followed (Mir and Pandey, 2018). 0.1 mg of synthesized powder was used for fabricating the working electrode. All

**Table 1**  
Synthesis parameters of Mo<sub>2</sub>C.

Sample Id	Reaction Temperature (°C)	Reaction Time (h)	Rate of heating (°C/min)	MoO <sub>3</sub> (g)	Mg (g)	Pipette tip (g)
PT1	600	10	5	1.4394	3.5	1
PT2	700	10	5	1.4394	3.5	1
PT3	800	10	5	1.4394	3.5	1
PT4	800	10	5	1.4394	3.5	0.25
PT5	800	10	5	1.4394	3.5	0.5
PT6	800	10	5	1.4394	3.5	0.75

the measurements were done with respect to the reference electrode reversible hydrogen electrode (RHE) immersed in an electrolyte solution of 0.5 M H<sub>2</sub>SO<sub>4</sub>. The high purity graphite rod was used as counter electrode. Linear sweep voltammetry (LSV) was performed in voltage range (−0.3 and 0.1 V) at 2 mVs<sup>−1</sup> scan rate. The chronoamperometry (CA) test were also done at constant potential for 10 h to check the stability of the catalyst. The cyclic voltammetry (CV) cycles were measured at (100 mVs<sup>−1</sup>) scan rate for 2000 cycles in (−0.3 to 0.2 V) voltage range. The CV plots in range 0.2–0.4 V at multiple scan rates were done to estimate the EDLC measurements. The electrochemical impedance spectroscopy (EIS) analysis was done at various potentials 50–550 mV in the frequency range 100 kHz–300 mHz. The CV plotted in voltage range (−0.3 to 0.3 V) at 50 mVs<sup>−1</sup> scan rate were done to remove contamination, activate surface of catalyst and stabilize the electrochemical currents before analysis.

### 3. Results and discussion

#### 3.1. X-ray diffraction (XRD)

Fig. 1a reveals the XRD plot for samples synthesized at various temperatures (600, 700 and 800 °C) for reaction time of 10 h. The PT1 shows the formation of molybdenum carbide (MoC) cubic phase, ICDD pattern (065–0280). The results reveal the formation of carburized product MoC at the relatively low temperature (600 °C). The typical XRD pattern of PT1 having broad diffraction peaks confirm the less crystallinity of the product phase. The results reveal the rapid reduction/carburization of MoO<sub>3</sub> in presence of Mg and carbon source (pipette tip) inside the autoclave (Mir et al., 2017). From this result it is concluded that the reaction temperature is not sufficient enough to form the crystalline Mo<sub>2</sub>C phase.

Increasing the temperature to 700 °C for 10 h (PT2) reveals the formation of Mo<sub>2</sub>C phase (ICDD reference 035–0787) as shown in Fig. 1a. The X-ray diffraction peaks correspond to the (100), (002), (101), (102), (110), (103), (200), (112) and (201) planes at positions 34.4, 37.9, 39.4, 52.1, 69.5, 74.5 and 75.5°, respectively. The extra peak at 26.6 corresponds to carbon (hexagonal, ICDD card 026–1076) as shown in (Fig. 1a), which attributes to crystalline carbon formed inside the autoclave and deposited on Mo<sub>2</sub>C surface at relatively higher temperatures. Further increasing the temperature to 800 °C (PT3), highly intense peaks of Mo<sub>2</sub>C phase shown in Fig. 1a, as a result of enhanced carburization at higher temperatures was observed. Moreover, the intensity of carbon peak also increased showing more crystallization of carbon at higher temperatures (Alhajri et al., 2014).

In order to optimize the initial carbon content on Mo<sub>2</sub>C phase formation at 800 °C for 10 h, the variation in the amount of initial carbon content was done as given in Table 1. Fig. 1b depicts the typical XRD pattern for samples prepared at 800 °C for fixed reaction time of 10 h with variation in carbon content. The PT4 in which the carbon source was 0.25 g, shows the formation of Mo<sub>2</sub>C along with impure phase Mo (ICDD reference 089–5023) as shown in (Fig. 1b). It reveals that the reduction has accomplished at this stage. However, the amount of carbon or the carbonaceous gases so generated are not optimum for carburization of Mo to Mo<sub>2</sub>C phase. Increasing the carbon content to 0.5 g (PT5) shows the formation of Mo<sub>2</sub>C phase (Fig. 1b) along with the diffraction peaks of Mo and an intermediate Mo<sub>0.42</sub>C<sub>0.58</sub> (ICDD pattern 036–0863), which also shows the reduction of MoO<sub>3</sub> has accomplished. However, the amount of carbon is not enough to convert reduced Mo and the intermediate phase (Mo<sub>0.42</sub>C<sub>0.58</sub>) to Mo<sub>2</sub>C. The amount of carbon source although higher than the stoichiometric value does not favor the complete carburization of MoO<sub>3</sub> (Dang et al., 2015; Zhao et al.,

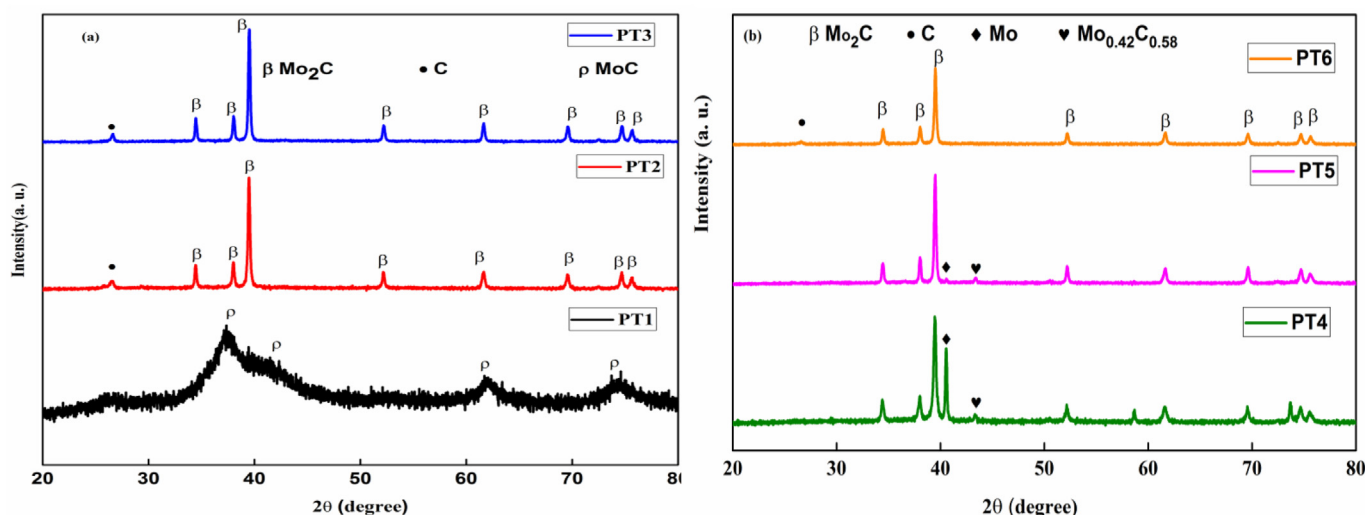


**Fig. 1.** XRD pattern of the synthesized samples (a) variation in temperature and (b) variation in carbon content.

2015). The sample PT6 (0.75 g of carbon) shows the formation of single phase Mo<sub>2</sub>C (035–0787) as depicted in (Fig. 1b). The peak intensity for the diffraction pattern is little lower as that attained at same temperature and time with 1 g of initial carbon content (PT3). Moreover, no diffraction peak corresponding to carbon shows the accomplishment of carbon content for formation of the product phase. The results predict that the 0.75 g of carbon concentration is optimum for formation of Mo<sub>2</sub>C phase. While as the 1 g of carbon at the same synthesis conditions shows the formation of Mo<sub>2</sub>C and residual free carbon. Higher the amount of carbide carbon concentration in Mo lattice, more is the platinum like behavior of the product (Choi et al., 2000).

The XRD results of (PT2, PT3 and PT6) reveal the formation of pure Mo<sub>2</sub>C phase having hexagonal structure (ICDD-035-0787). To verify the crystal structure of the pure phase Mo<sub>2</sub>C, the XRD data has been fitted via Rietveld refinement for hexagonal space group (P6<sub>3</sub>/mmc) with Wyckoff positions for Mo and C as given in literature (El and Parth, 1963). The fitted Rietveld refinement plots of the synthesized products (PT2, PT3 & PT6) are depicted in (Fig. S2a–c, SI). The  $\chi^2$  values, lattice parameters of the analyzed samples and the site occupancy of Mo and C so estimated is given in Table S1. The PT2 and PT3 shows nearly stoichiometry of Mo and C. However, the PT6 shows the 30% C vacancy in the lattice of Mo<sub>2</sub>C. The crystal structures generated from Rietveld fit for the hexagonal system of PT3 is shown in Fig. 2d, (SI). The amount of carbon in Mo<sub>2</sub>C lattice is a function of initial carbon content. It generates the higher carbon gradient to favor diffusion of C in Mo lattice through surface diffusion. In this process carbon network forms on the surface of particle, which further hinder the diffusion of carbon in Mo lattice.

The crystallite size estimated from Scherrer criterion is given in (Table S1) (Lad and Pratap, 2006). The estimated crystallite size of PT1 is very small, which is attributed to peak broadening. For Mo<sub>2</sub>C phase it shows a decreasing pattern with temperature as given in Table S1, (SI). It enhances with increase in carbon content followed by decrease as given in Table S1, (SI). The strain induced in the synthesized samples as a result of carburization affects the peak broadening. Williamson–Hall (W–H) study estimates the strain induced in the synthesized samples. Mir et al. (Mir et al., 2017) represented detailed mathematical formulas of different W–H models, for hexagonal systems. For cubic systems the calculations were done with the help of expression given in literature (Krasnenko and Brik, 2012). The MoC (PT1) phase shows lower crystallite size and more strain. It might be because of the intermediate phase formation at low temperature. The quality of the fit for (100) of PT2 is depicted in Fig. S3a, (SI). The crystallite size has implied decreasing trend with increase in the temperature given in (Tables S1 and SI) for PT3 and PT2, respectively. The results are in agreement with full width at half maxima (FWHM), which shows an increase with rise in temperature as presented in Fig. S3a–b, (SI). The Scherrer plot for PT2 with  $(1/\beta)$  on x-axis and  $\cos\theta$  on y-axis is shown in Fig. S3c, (SI). These models were fitted and the uniform strain energy density model (USEDM) seems to be more appropriate having better quality of fit ( $R^2 = 0.99$ ) than uniform strain deformation model (USDM,  $R^2 = 0.98$ ) and uniform strain model (USM,  $R^2 = 0.96$ ) as depicted in (Fig. S2d–f, SI), respectively. The estimated results are tabulated in (Tables S1 and SI). The crystallite size calculated from the USM, USDM and USEDMD are consistent. The strain estimated from W–H analysis shows decreasing trend with increase in temperature. The prominent peak of carbon in PT3 compared to PT2 indicates that the diffusion of carbon at higher temperature got saturation value and lattice carbon gets relaxed leading to low strain value. However, the higher strain value in PT4 might be due to the presence of more Mo intermediate phase, which has not attained equilibrium because the amount of carbon

is not sufficient enough for the formation of pure Mo<sub>2</sub>C phase. The carbon content gradient might be a reason for strain induction in the product phase. However, further increasing the carbon content, PT5 shows a different pattern of strain estimation. The strain generated in PT5 is less as compared to PT4, because of the higher carbon content gradient than PT4, which favors the diffusion of C in Mo lattice and lowers the strain. Brar et al. (2016) also observed a different pattern in strain analysis below 5.5 (molar ratio) carbon concentration. Increasing the initial carbon content (PT6) shows the increase in strain value because of pure phase formation of Mo<sub>2</sub>C with no extra carbon peak in XRD pattern (Fig. 1b). The results predict that carbon in PT6 is accomplished to form Mo<sub>2</sub>C. Due to strong interaction between Mo and carbon on the surface, the product phase in PT6 remains in the higher strained state, because of the low carbon on the surface. However, strain induced in PT3 is lower as compared to PT6 where the extra carbon formed on surface of Mo<sub>2</sub>C helps in retaining the stable state of product phase with lower strain (Brar et al., 2016).

### 3.2. Morphological studies

The FESEM micrographs of the synthesized samples (PT1, PT2, PT3 and PT6) are shown in (Fig. S4 a–e, SI). Structural analysis reveal that the particles are agglomerated having tubular to faceted morphology for PT1 and PT2 as depicted in Fig. S4 a&b, (SI), respectively. However, PT3 shows the different morphological features where presence of graphene sheet and agglomerated particles can be seen (Fig. S4 c, SI). Higher magnified image (Fig. S4 d, SI) shows that most of the particles are embedded in graphene sheets. In sample PT6 (Fig. S4 e, SI) agglomerated particles are observed. The structural variation is observed because of variation in synthesis parameters. The EDS analysis shown in Fig. S5 a–d, (SI) reveals the presence of C, Mo and O elements, where carbon content is higher for PT3 as given in Table S2, (SI).

The TEM analysis of PT1 shows the formation of MoC phase embedded inside the tubular carbon network as shown in Fig. S6a, (SI). The SAED pattern confirms the MoC phase having d-spacing 0.24 and 0.15 nm corresponding to (111) and (220) plane consistent with ICDD pattern 065–0280. In PT2 sample particles having spherical to faceted morphology encapsulated in carbon matrix were observed as shown in Fig. S7a, (SI). The high resolution TEM (HRTEM) micrograph (Figs. S7b and SI) and SAED pattern (Figs. S7c and SI) confirmed the incorporation of the Mo<sub>2</sub>C in carbon cloth. These results are consistent with XRD reference (ICDD-035-0787) for Mo<sub>2</sub>C and carbon (ICDD pattern-026-1076). The coating in TEM image of PT6 (Figs. S8a and SI) is little thinner, which is in agreement with experimental parameters. The HRTEM and SAED pattern confirms the Mo<sub>2</sub>C phase formation enclosed in the graphitic carbon layer as shown in Fig. S8b and S8c, (SI) consistent with XRD pattern. In PT3 faceted Mo<sub>2</sub>C particles embedded in graphene sheet can be seen in Fig. 2a. These faceted structure having thick carbon coating form the layered structure (Fig. 2b). The HRTEM (Fig. 2c) and SAED pattern (Fig. 2d) confirms the graphitic carbon coated Mo<sub>2</sub>C as the final carburized product consistent with ICDD reference pattern of carbon and Mo<sub>2</sub>C, respectively.

### 3.3. X-ray photoelectron spectroscopy (XPS)

The surface chemistry analysis and the chemical composition of the pure phase synthesized samples (PT3 and PT6) were determined by XPS. The overall survey spectrum of the PT3 and PT6 are given in (Fig. 3a and b), respectively. It precisely shows the presence of Mo, O and C, respectively. The peak positions at binding energy (BE) 231.4, 284.5, 396.8, 412.9 and 531.4 eV correspond to Mo3d, C1s, Mo3p<sub>5/2</sub>, Mo3p<sub>3/2</sub> and O1s, respectively (Gao et al., 2014). The



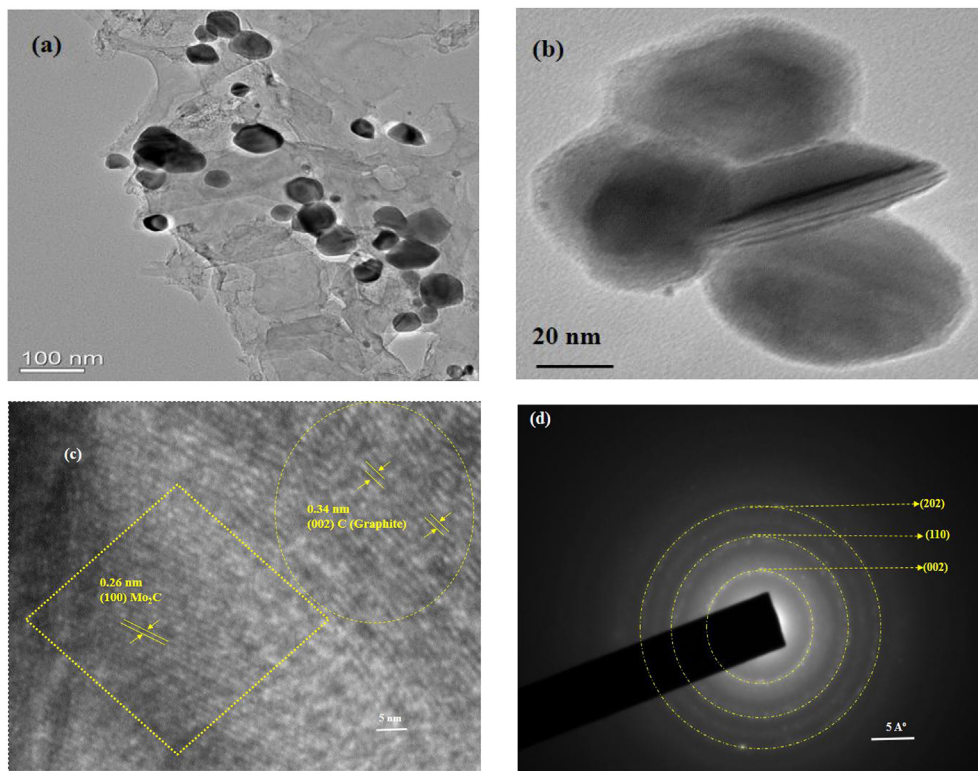


Fig. 2. Micrographs of PT3 ( $\text{Mo}_2\text{C}$ ) (a) TEM, (b) magnified image of TEM, (c) HRTEM and (d) SAED pattern of  $\text{Mo}_2\text{C}$ .

high resolution spectra of PT3,  $\text{Mo}3d$  (Fig. 3c) depicts the presence of  $\text{Mo}3d_{5/2}$  (2+) and  $\text{Mo}3d_{3/2}$  (2+) bonded to  $\text{Mo}_2\text{C}$  at positions 228.3 and 231.6 eV, respectively (Shi et al., 2017). The peaks having BE 232.5 and 235.7 eV correspond to  $\text{Mo}3d_{5/2}$  (6+) and  $\text{Mo}3d_{3/2}$  (6+), respectively, which is attributed to oxidation of  $\text{Mo}_2\text{C}$  surface in air or prolonged duration during XPS analysis (Alhajri et al., 2014). The spectra of PT6  $\text{Mo}3d$  shown in (Fig. 3d) reveal the formation of product phase  $\text{Mo}_2\text{C}$  due to presence of  $\text{Mo}3d_{5/2}$  (2+) and  $\text{Mo}3d_{3/2}$  (2+) species at BE positions 228.5 and 231.3 eV. The indication of enriched electron around Mo in  $\text{Mo}_2\text{C}$  was confirmed by shift in BE of  $\text{Mo}2+$  towards lower side (Shi et al., 2017). The peaks having BE of 232.5 and 235.7 eV correspond to  $\text{Mo}3d_{5/2}$  (6+) and  $\text{Mo}3d_{3/2}$  (6+), respectively as a result of oxidation of  $\text{Mo}_2\text{C}$  to form  $\text{MoO}_3$  (Alhajri et al., 2014). The  $\text{C}1s$  spectra of PT3 and PT6 are given in (Fig. S9a&c, SI), the peaks  $\sim 284.4$  and  $\sim 285.2$  attribute to C–C (graphitic), respectively (Liu et al., 2015). In  $\text{C}1s$  spectra, the Mo–C (carbide) peak is inhibited by the carbon peak due to the excess surface carbon having similar BE region of C–C and Mo–C (Xiao et al., 2015). Moreover, the  $\text{O}1s$  spectra of PT3 and PT6 in (Fig. S9b&d, SI) shows the presence of surface molybdenum oxide species having BE 530.5, 531.2, 532.3 and 529.2, 530.2 and 530.7, respectively corresponding to Mo–O and C–O (Ding et al., 2016).

### 3.4. Raman spectroscopy

The Raman spectroscopy studies were done to estimate the graphitization of the synthesized products. The Raman spectrum of synthesized samples (PT1, PT2 and PT3) shown in Fig. 4a, exhibits the Raman peaks at positions given in Table 2. These correspond to the disorder induced D-band, G-band and 2D-band for the crystalline graphite, respectively (Ferrari, 2007; Ferrari and Robertson, 2000). The ID/IG ratio (Table 2) of PT1, PT2 and PT3 is nearly same, which confirms the similar order of the carbon. The presence

of the 2D peak in PT2 and PT3 confirms that the synthesized sample are graphitic/graphene carbon supported species (Das et al., 2008). The increase in I2D/IG ratio (Table 2) confirms the increase in graphitization of carbon with temperature. The shifting of the 2D band towards  $(2690\text{ cm}^{-1})$  attributes to the transformation of highly pyrolytic graphitic carbon to graphene. The shift of G band peak about  $(10\text{ cm}^{-1})$  attributes to the self-doping defects of in-situ carbon coated  $\text{Mo}_2\text{C}$  phase (Das et al., 2008). The increase in I2D/IG correspond to increase in graphene layers with temperature.

The Raman spectra for the synthesized samples PT4, PT5 and PT6 with variation in initial carbon content is shown in Fig. 4b and the corresponding bands so obtained are given in Table 2. Low intensity peak at  $\sim 658.2$  corresponds to (Mo–O–Mo stretch) of molybdenum oxide species (Mo et al., 2015). The presence of highly intense peak at position  $817.2\text{ cm}^{-1}$  is (Mo=O stretch) and the peak at  $\sim 987\text{ cm}^{-1}$  belongs to  $\text{MoO}_3$  species (Mo et al., 2015). Moreover, the PT4 (Fig. 4b) shows no sign of D and G bands confirming 0.25 g carbon source is not sufficient to have surface carbon. The oxide species so obtained in Raman spectra of PT4 may be due to some oxide content present in the sample as the phase transformation from oxide to carbide has not occurred completely and is beyond the determination limit of XRD. The Raman spectra of the PT5 sample follows the same trend with decreasing intensity of molybdenum oxide species peaks and shows the presence of D, highly intense G and 2D band at positions (Table 2) shown in Fig. 4b. The molybdenum oxide species may correspond to inherently retained oxide. The surface carbon prevents the oxidation of the  $\text{Mo}_2\text{C}$  surface, which results in a decreased intensity of Mo oxide species as compared to PT4. However, the PT6 sample only shows the presence of D, G and 2D band in Raman spectra at positions given in Table 2 and shown in Fig. 4b. The peak positions shift towards higher wave number as compared to PT5. The decrease of peak intensity for D and G bands in PT6 as compared to PT5 may be due

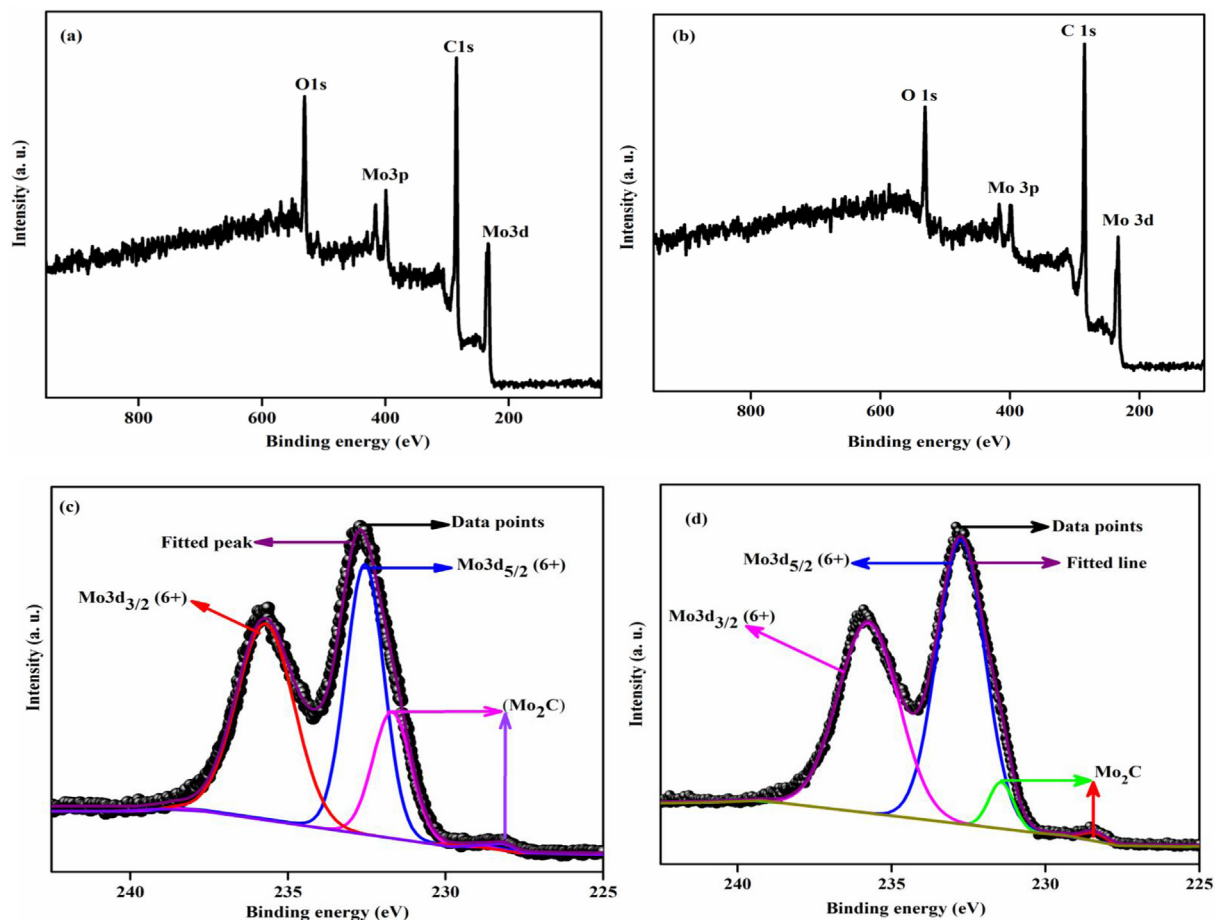


Fig. 3. XPS spectra of (a) Survey spectra of PT3, (b) Survey spectra of PT6, (c) HR spectra of Mo3d of PT3 and (d) HR spectra of Mo3d of PT6.

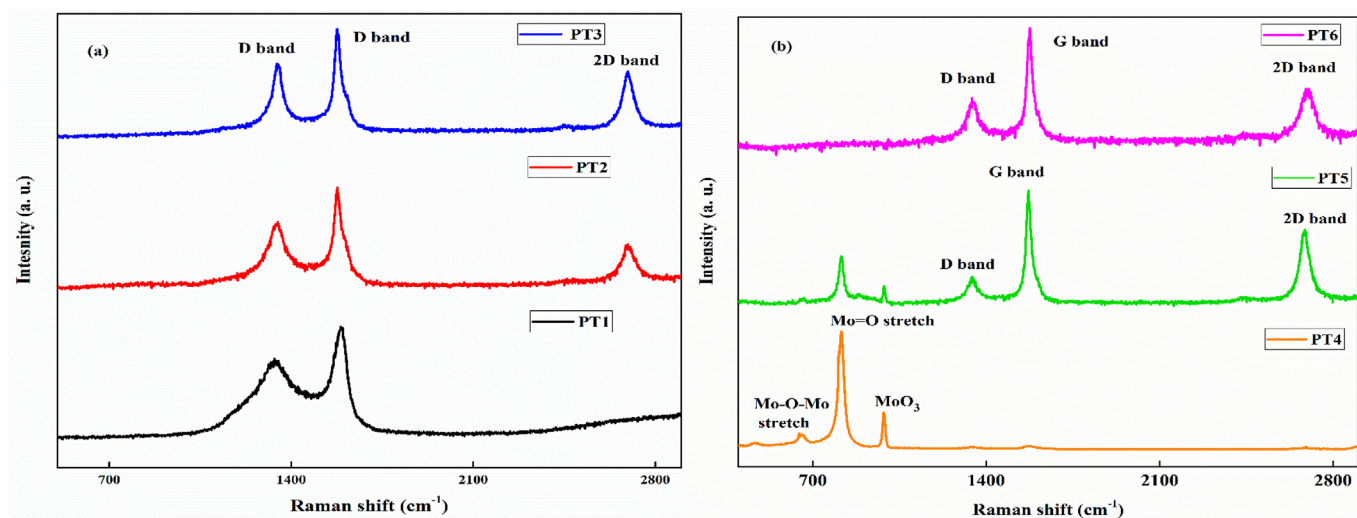


Fig. 4. Raman spectra of (a) PT1, PT2 and PT3 and (b) PT4, PT5 and PT6.

to utilization of more carbon to accomplish the phase formation of  $\text{Mo}_2\text{C}$ . The shifting of the 2D peak from 2684.7 to 2701.5 reveals the formation of graphene in carbon support. The ID/IG and I2D/IG of PT6 is lower than PT3, which shows the presence of higher disorder and graphitized carbon species, respectively (Ferrari and

Robertson, 2000). The results are in well agreement with the formation of more carbon support over  $\text{Mo}_2\text{C}$  surface with increase in initial carbon content as observed by XRD and microstructural analysis.

**Table 2**  
Raman spectroscopy parameters.

Sample Id	D band		G band		2D band		ID/IG	I2D/IG
	Peak position (cm <sup>-1</sup> )	Intensity (a. u)	Peak position (cm <sup>-1</sup> )	Intensity (a. u)	Peak position (cm <sup>-1</sup> )	Intensity (a. u)		
PT1	1334.3	8779.2	1590.3	12468.1	—	—	0.7	—
PT2	1344.9	3735.4	1579.6	5452.8	2693.1	2738.7	0.69	0.5
PT3	1350.7	6116.3	1590.3	8582.7	2691.6	5779.2	0.71	0.67
PT4	—	—	—	—	—	—	—	—
PT5	1339.1	2306.7	1569.7	6942.2	2684.7	4764.2	0.33	0.68
PT6	1346.6	1584.6	1571.3	3331.1	2701.5	1889.2	0.48	0.57

### 3.5. Thermogravimetric analysis (TGA)

TGA for the synthesized powders have been performed from room temperature to 1000 °C under flowing air to estimate the thermal stability and chemical composition. The expected mass loss may attribute to the oxidation of carbon residue, while as the oxidation of Mo<sub>x</sub>C (x = 1, 2) species lead to mass gain. The TGA analysis of the synthesized samples (PT1, PT2 and PT3) is depicted in Fig. S10a, (SI). The initial mass loss of about 1% is observed for all the synthesized samples that correspond to the absorbed water on the surface. The mass gain of about 7% in PT1 confirm the oxygen incorporation in MoC to form MoO<sub>x</sub>C<sub>y</sub>. The weight loss about 10% in between 376 and 467 °C corresponds to the combustion of carbon releasing CO and CO<sub>2</sub>. The slight mass gain thereafter till 535 °C attributes to the oxidation of remaining MoC and MoO<sub>x</sub>C<sub>y</sub> to form MoO<sub>3</sub> (Pang et al., 2010). The straight line till 715 °C determines the stability of the formed product. The weight decreases gradually thereafter, but the decrease is slow till 800 °C. The rapid mass loss thereafter is in accordance with the evaporation of MoO<sub>3</sub> (Chen et al., 2011). The straight line TGA curve of carbon coated Mo<sub>2</sub>C (PT2 and PT3) in Fig. S10a, (SI) shows higher thermal stability as compared to MoC (PT1) in temperature range 308 °C and 315 °C, respectively. The slow mass gain till 438 and 363 °C in case of the PT2 and PT3 designate the oxidation of Mo<sub>2</sub>C species, respectively (Wang et al., 2015). Both the mass gain and loss occur simultaneously because of oxidation of carbide and carbon species. The mass gain till 128 and 130% at peak points 572 °C and 555 °C attributes to oxidation of Mo<sub>2</sub>C to MoO<sub>3</sub>. The result shows almost straight line till 444 °C in PT3, indicating a thicker graphitic carbon layer, which inhibits rapid oxidation of Mo<sub>2</sub>C. The formation of oxide layer in temperature range (363–444 °C) also enhances stability of the product phase. The samples show mass loss as a result of oxidation/combustion of carbon residue up to temperature range of 720 °C (Pang et al., 2010). The sudden and rapid mass loss thereafter is attributed to the evaporation of molybdenum oxide phase (Alhajri et al., 2014).

The TGA for samples (PT4, PT5 and PT6) is shown in Fig. S10b, (SI). The mass gain trend in TGA curve of PT4 and PT5 (till 350 °C) shows the oxidation of Mo species in the synthesized product. The sudden increase in mass may be the result of less extra carbon in the sample to inhibit the oxidation process. The rapid mass gain till 530 and 565 °C for PT4 and PT5 (139%) results from oxidation of Mo and Mo<sub>2</sub>C species, respectively. The TGA curve remains constant for PT4 from 530 to 810 °C, which reveals the stability of the MoO<sub>3</sub> and intermediate molybdenum oxide. The slight variation in mass gain trend (PT5) might be a reason of complex oxidation of Mo<sub>2</sub>C and carbon residue present in the system. The slight decrease in mass variation may be a result of combustion of carbon residue because of the higher initial carbon content in PT5 compared to PT4 that shows change in TGA pattern till 715 °C. The mass loss from 715 to 750 °C is attributed to the evaporation of formed MoO<sub>3</sub>. However, the stable curve till 810 °C may due to comproportion of intermediate molybdenum oxide species stable within this temperature

range. The rapid mass loss after 810 °C reveals the evaporation of the formed MoO<sub>3</sub> phase. The PT6 sample shows the trend comparable to PT3 and PT2 showing stability till 482 °C after releasing the absorbed water. The slight change from (350–482 °C) in TGA curve (Figs. S10b and SI) may be due to the oxidation of residual surface carbon followed by the formation of oxide layer. The mass increases sharply up to 736 °C as a result of oxidation of Mo<sub>2</sub>C to MoO<sub>3</sub>. The sample shows higher thermal stability as compared to PT3, PT4 and PT6, respectively. The mass decrease till 840 °C may be the result of oxidation of carbon residue as discussed and then shows a decreasing trend corresponding to evaporation of MoO<sub>3</sub>. The PT6 results suggest higher amount of Mo<sub>2</sub>C phase as observed by mass gain above 550 °C (Alhajri et al., 2014). The oxidation of molybdenum carbide (Mo<sub>x</sub>C x = 1,2) and incorporated carbon species is a complex process as determined by the TGA analysis.

The composition of sample was estimated from mass change analysis, assuming only carbon coated Mo<sub>2</sub>C in samples and MoO<sub>3</sub> as solid combustion product. The free carbon in all the synthesized samples is calculated by Equations S1 and S2 (SI), respectively (Thomas-Garcia et al., 2014) (Brar et al., 2016). The results so obtained are given in Table 3. The estimated free carbon content is higher in PT3 and lowest in PT4, which is in accordance with the experimental parameters. Though the initial carbon content in PT1, PT2 and PT3 is same, however, in the final product the free carbon content varies with synthesis temperature. It might be due to less graphitization of hydrocarbon gases in low temperature range, which is in accordance with microstructural and Raman analysis.

### 3.6. Brunauer–Emmett–Teller (BET) analysis

The BET specific surface area (SSA) for the synthesized samples was estimated by nitrogen (N<sub>2</sub>) adsorption/desorption studies. The adsorption-desorption isotherms presented in (Figs. S11a and SI) demonstrate type II isotherm due to porous nature of carbon coated Mo<sub>2</sub>C composites (Lee et al., 2014). The estimated values of BET SSA of the synthesized powders are given in (Table 3). The PT1 sample reveals the higher BET SSA, which is in correlation with the lower crystallite size estimated from XRD analysis. However, the surface area has shown decreasing trend with the increase in temperature tabulated in Table 3. The pore size estimated from BET analysis increases, while the pore volume depicted decreasing trend with the increase in temperature (Table 3). The BET SSA has decreased with the increase in temperature, which corresponds to sintering of the powder surfaces at higher temperatures (Wu et al., 2013). The increase in SSA from PT4 to PT5 might be the result of more porous nature of PT5 having a mean pore size of 8 nm as revealed in (Figs. S11b and SI). The SSA decreases from PT5 to PT6 with increase in carbon content. The highly dense crystalline nature of carbon around Mo<sub>2</sub>C may result in lowering of BET SSA (Wu et al., 2013). The pore size distribution of PT6 (Fig. S11 c, SI) shows wider pore size distribution and lower pore volume as given in Table 3. The decrease in pore volume with increase in carbon content (PT5 to PT6) might be because of the pore strain and pore rupture at higher



**Table 3**

Carbon content estimation from TGA, BET estimated parameters and electrochemical results of the synthesized samples.

Sample Id	% Free carbon (TGA)	BET SSA ( $\text{m}^2\text{g}^{-1}$ )	Pore volume ( $10^{-3}\text{cm}^3\text{g}^{-1}$ )	Pore diameter (nm)	Tafel slope (b) $\text{mVdec}^{-1}$	EDLC ( $C_{dl}$ ) $\text{mFcm}^{-2}$
PT1	67.0	40.7	22.2	4.0	122.4	1.2
PT2	72.0	11.0	38.5	14.0	93.9	3.5
PT3	76.6	6.6	27.3	16.7	82.6	19.45
PT4	50.0	9.3	39.5	17.0	101.5	0.3
PT5	56.6	37.1	74.8	8.0	122.2	1.75
PT6	65.9	7.9	10.2	5.2	80.1	12.2

temperatures (Rather et al., 2017a). The agglomeration of the pure phase  $\text{Mo}_2\text{C}$  particles encapsulated in dense carbon matrix in PT3 and PT6 results in lower surface area (Rather et al., 2017b).

### 3.7. Electrochemical studies

#### 3.7.1. HER activity

The HER activity of prepared samples of carbon coated MoC (PT1) and  $\text{Mo}_2\text{C}$  (PT2 & PT3) were analyzed by linear sweep voltammetry (LSV) measurements at a scan rate of  $2\text{ mVs}^{-1}$ . The polarization curves corresponding to PT1, PT2 and PT3 are shown in Fig. 5a. The current density of PT1 is  $34\text{ mAcm}^{-2}$  and those of PT2 and PT3 are  $15.4$  and  $27.2\text{ mAcm}^{-2}$ , respectively. The more value of current density in MoC (PT1) is attributed to small crystallite size as calculated from XRD analysis and higher BET specific surface area (Zhong et al., 2016). The transport path ways of electrolyte ions is

enhanced by the smaller size of the particles. The current density is less in PT2 as compared to the PT1, which may be the result of larger crystallite size, less BET specific surface area and incorporation of the agglomerated  $\text{Mo}_2\text{C}$  particles in the carbon matrix. The PT3 shows enhanced current density values (Fig. 5a) as compared to PT2. This may be due to the decrement in crystallite size and surface carbon graphitization, which improves the charge transfer kinetics on  $\text{Mo}_2\text{C}$  surface (Li et al., 2016). The increase in synthesis temperature (PT2 to PT3) results in improvement of current density. The synthesis conditions leading to variation in nature of surface carbon affects the charge kinetics of  $\text{Mo}_2\text{C}$  surface, which influences the current density values (Zhong et al., 2016). The temperature dependent strain generated in the lattice shows variation in d-band structure and thus affects HER activity (Sun et al., 2018). The PT4 having  $\text{Mo}_2\text{C}$  as major and Mo as impurity phase and the PT5 having  $\text{Mo}_2\text{C}$  as major, Mo and  $\text{Mo}_{0.42}\text{C}_{0.58}$  as

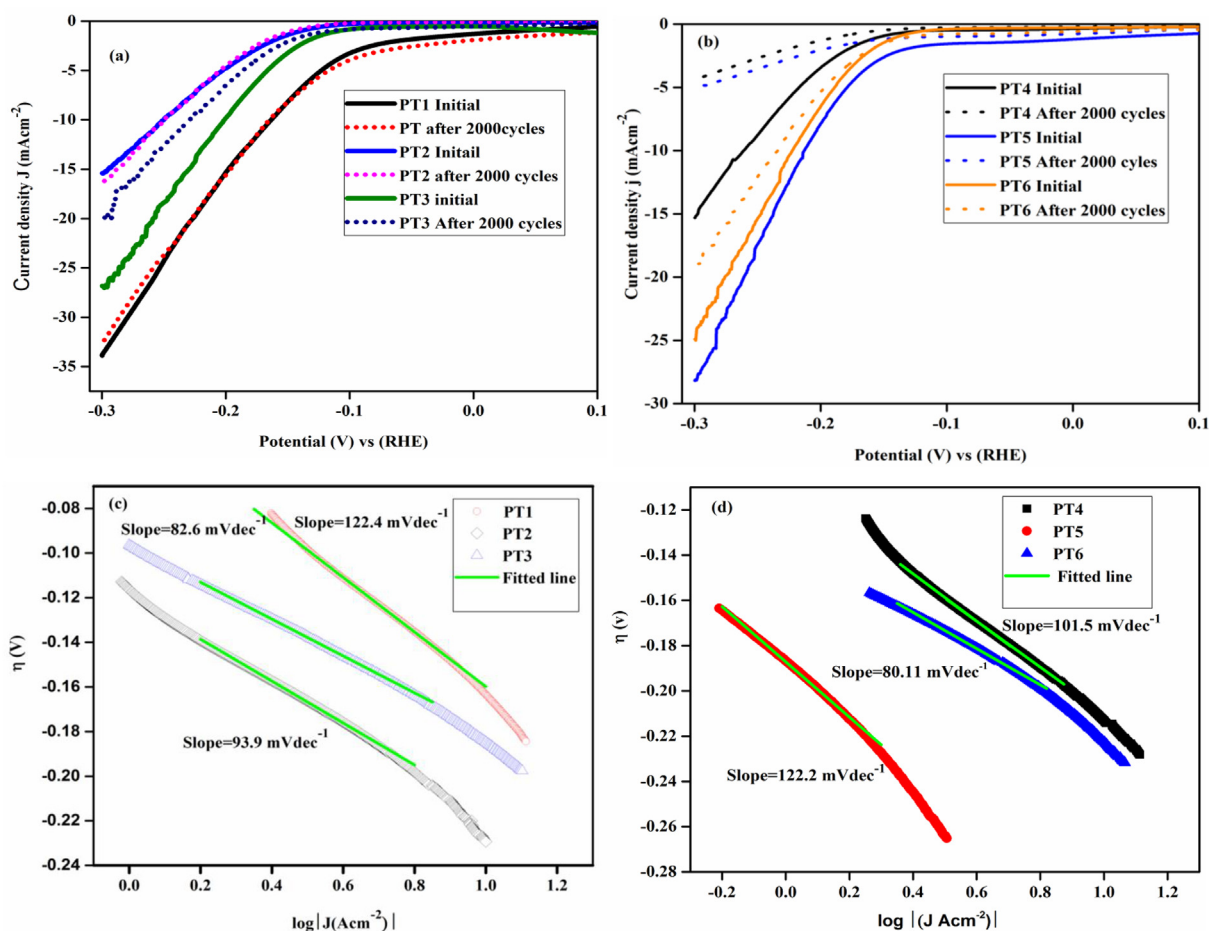
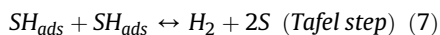
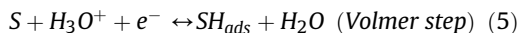


**Fig. 5.** Electrochemical measurements (a) Linear voltammetry plots PT1, PT2 and PT3, (b) Linear voltammetry plots PT4, PT5 and PT6, (c) Tafel plot of PT1, PT2 and PT3, (d) Tafel plot of PT4, PT5 and PT6.



minor impurity phases shows the current density of 16 and 27.5 mAcm<sup>-2</sup>, respectively as given in Fig. 5b. The lower current density value obtained in PT4, although having low value of crystallite size as compared to PT5 might be the result of low carbon content in the sample. The PT5 having higher value of extra carbon as compared to PT4 as evidenced from Raman and TGA, shows higher surface area and thus enhances the current density values as depicted in Fig. 5b. The presence of molybdenum oxide species as evidenced from the Raman analysis being less electrochemically active candidates also decreases the current density values. The results also predict increase in the current density with more Mo<sub>2</sub>C content in the prepared samples. The result of PT4 and PT5 confirms that Mo is not an active electrocatalyst. The incorporation of C in Mo lattice makes it active electrocatalyst because of resemblance of d-band structure with Pt (Michalsky et al., 2014; Levy and Boudart, 1973). The pure phase Mo<sub>2</sub>C (PT6) shows current density of 25.0 mAcm<sup>-2</sup> (Fig. 5b). The higher value of current density might be because of the pure phase formation of Mo<sub>2</sub>C and presence of extra carbon content in product. The conductive carbon layer as confirmed by Raman spectroscopy and TEM in between the particles facilitate the electron transfer and enhance the conductivity between the Mo<sub>2</sub>C particles. The molybdenum carbide particles embedded in carbon matrix exhibit them from agglomeration and activates more exposed sites (Li et al., 2016).

To discern the mechanism responsible for HER activity, the Tafel slope (b) an immanent characteristics of the electrocatalyst was estimated from Tafel plot designated in (Table 3) and shown in (Fig. 5 c-d). The HER mechanism follows the following steps:



where S' is an active site and SH<sub>ads</sub> is the hydrogen adsorbed on that particular site. The Volmer reaction (5) is rate determining step, if the value of b is up to 120 mVdec<sup>-1</sup>. The Heyrovsky (6) and Tafel (7) reactions determine the rate of reaction step, if the value of b is about 40 and 30 mVdec<sup>-1</sup>, respectively. The Tafel slope (b) of PT1 is 122.4 mVdec<sup>-1</sup>, which is comparable to 120 mVdec<sup>-1</sup>. The results predict the rate determining step for HER activity is Volmer reaction. The value of (b) for PT2 and PT3 (Fig. 5c) are 93.9 and 82.6 mVdec<sup>-1</sup>, respectively and also predicts that Volmer step is rate determining for HER. The hydrogen bubble produced on the surface of the working electrode is shown in Fig. S1, (SI). The low value of b compared to PT1 might be the result of pure phase formation of Mo<sub>2</sub>C, which is more efficient electrocatalyst for HER. The transformation of the order of the residual free carbon with synthesis temperature enhances the electrical conductivity, hydrogen adsorption and improves the HER activity. The Tafel slope (b) for PT4, PT5 and PT6 are 101.5, 122.2 and 80.11 mVdec<sup>-1</sup>, respectively (Fig. 5d). The higher value of (b) for PT4 determines weak adsorption on electrocatalyst surface, because of low initial carbon content and negligible surface carbon as estimated from Raman analysis. The higher value of (b) for PT5 as compared to PT4 might correspond to lattice distortion calculated from W–H analysis, which affects covalent properties, surface atomic arrangements and electron occupation states (Daio et al., 2015; Ma et al., 2014). The Tafel slope of (b) for PT6 shows that reaction (5) proceeds faster as compared to PT4, PT5 and PT2. The results of PT3 and PT6 are comparable and depends on the thickness of graphitic carbon content that enhances the charge transfer kinetics.

For HER performance, the stability of the synthesized samples is

an imperative parameter. The stability of the product phases has been determined by cyclic voltammetry (CV) analysis in acidic medium for 2000 cycles in voltage window (0.2 to –0.3 V) at a scan rate of 100 mVs<sup>-1</sup>. The LSV performed after 2000 CV cycles for PT1 shows negligible loss of current density depicted in Fig. 5a. The higher stability may be due to surface carbon, which inhibits the degradation/corrosion of the synthesized product during HER activity. The LSV measurements of PT3 as compared to PT2 shows similar polarization curves with loss of current by 23%, respectively (Fig. 5a). This shows that PT2 is more stable as compared to PT3. The stability of PT2 and PT3 is influenced by the nature of surface carbon. The less graphitic carbon in PT2 as compared to PT3 enhances the stability of the product although the current density is low (Zhang et al., 2015). The higher free carbon as estimated from TGA enhances the current density in PT3, but during testing the catalyst destabilizes because of the porous structure of carbon. The excessive carbon in the carburized product may also cover some of the active sites and deteriorate the HER activity. The PT4 and PT5 sample lose their efficiency with maximum loss of current in the given range as implied in (Fig. 5b). The presence of more Mo phase in PT4 could lead to oxidation/corrosion of the product surface to form a less electro active species and diminishes its efficiency. The PT5 shows higher initial current density, but its stability is comparable to PT4 after 2000 CV cycles as depicted in Fig. 5b. The destabilization of PT4 and PT5 could be a result of oxidation/corrosion of Mo<sub>2</sub>C and Mo species in acidic medium because of the low surface carbon content. However, PT6 sample shows the loss of current by 23% as shown in Fig. 5b, which is more stable than PT4 and PT5 but the results are comparable to PT3. The results predict that the amount of initial carbon content 0.75 and 1.0 g for its synthesis shows the similar results for HER activity. The stability of pure phase Mo<sub>2</sub>C (PT2, PT3 and PT6) incorporated in carbon matrix were also done by chronoamperometry (CA), the results are depicted in Fig. S12, (SI). The results reveal the stability of 10 h at a constant potential (170 mV) with negligible loss of current and predict that pure Mo<sub>2</sub>C particle in carbon encapsulation is stable electrocatalyst for HER. The high durability of the electrocatalyst synthesized at relatively lower temperatures originates from the bonding characteristics of surface carbon and enclosed Mo<sub>2</sub>C particles developed during in-situ synthesis. The deviation from straight line of CA (Figs. S12 and SI) for PT6 might correspond to surface carbon thickness and carbon vacancies. The results reveal that most stoichiometric phase of Mo<sub>2</sub>C as calculated from the Rietveld refinement (PT2) shows low current density and higher stability as compared to carbon vacant phase (PT3 and PT6), having enhanced current density and relatively low stability. The results reveal the vacancy of carbon within the synthesized species enhances the charge transfer rate and the strain developed affects the stability characteristics. However, the nature of in-situ developed surface carbon and its thickness needs to be optimized at lower temperatures to enhance the efficiency and activity of electrocatalyst.

### 3.7.2. Electrochemical double layer capacitance (EDLC, C<sub>dl</sub>)

The EDLC (C<sub>dl</sub>) analysis have been performed via CV at different scan rates (50–320 mVs<sup>-1</sup>) in a voltage range of 0.2–0.4 V depicted in (Fig. S13a–f, SI). The CV plots for the synthesized samples at a fix scan rate (320 mVs<sup>-1</sup>) are shown in Fig. 6a. The pure Mo<sub>2</sub>C phase incorporated in carbon matrix exhibit regular and sharp rectangular shape (Fig. 6a). This indicates enhanced electrochemical reversibility even at higher scan rates during the charge/discharge processes. The plots of scan rate (mVs<sup>-1</sup>) with current density Δj<sub>0.3</sub> (mAcm<sup>-2</sup>) is shown in Fig. 6b–c and the results are depicted in Table 3. The MoC (PT1) incorporated in carbon matrix shows the C<sub>dl</sub> value of 1.2 mFcm<sup>-2</sup> (Table 3). However, the Mo<sub>2</sub>C (PT2, PT3)

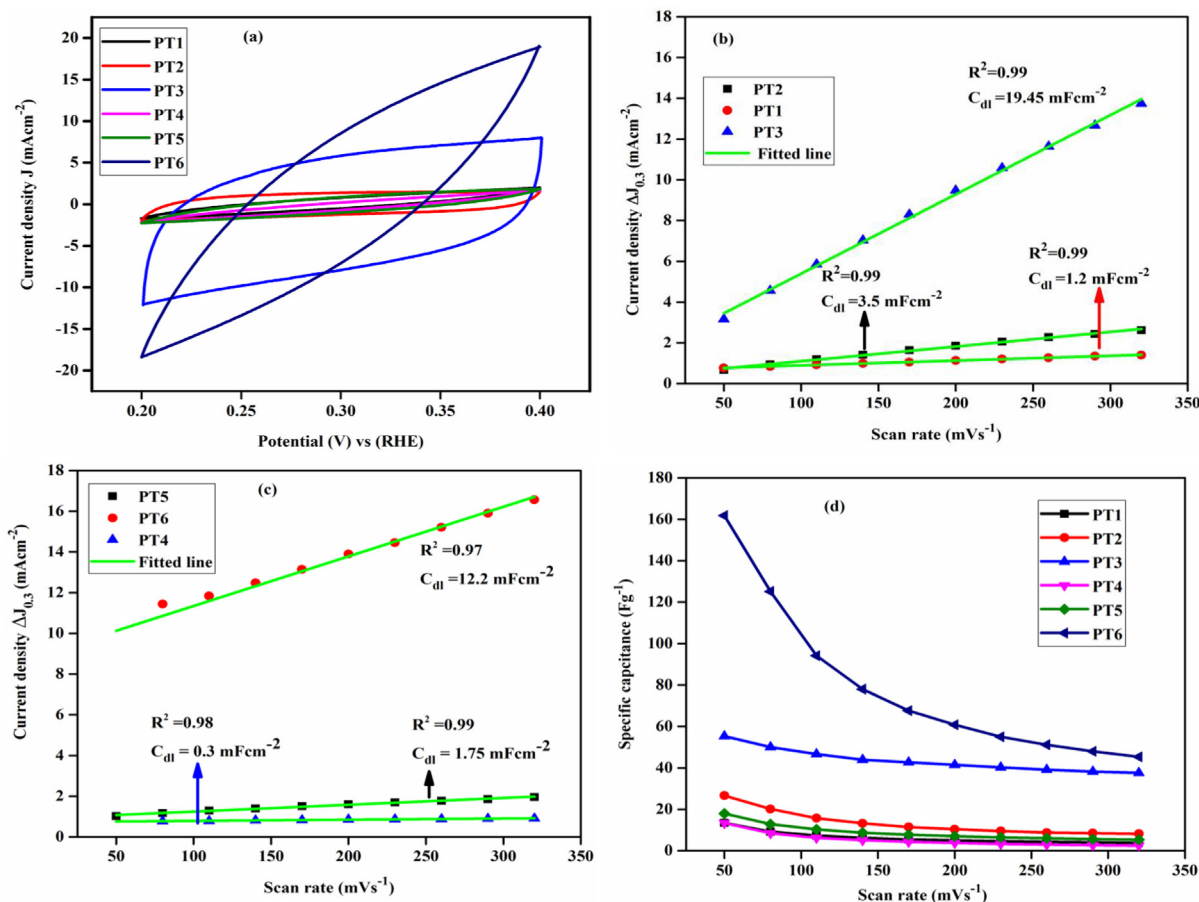


**Fig. 6.** (a) Cyclic voltammetry (CV) plots at 320 mVs<sup>-1</sup>, (b) Electric double layer capacitance of PT1, PT2 and PT3, (c) EDLC of PT4, PT5 and PT6 and (d) Specific capacitance at different scan rates.

encapsulated in carbon shows the  $C_{dl}$  of 3.5 and 19.46 mFcm<sup>-2</sup>, respectively. The results are in correlation with the shape of CV cycles towards rectangular pattern exhibiting enhanced charge storage capacity. The  $C_{dl}$  results estimated for PT3 are higher as compared to results obtained by Li et al. (2016). However, the CV of PT4 and PT5 also deviate from rectangular pattern. The higher value of  $C_{dl}$  for pure phase Mo<sub>2</sub>C could be result of fast charge separation of non-faradic process between the interface of electrode interface and electrolyte. The  $C_{dl}$  values obtained for PT4 and PT5 are 0.29 and 1.8 mFcm<sup>-2</sup>, respectively. The decrement in value of  $C_{dl}$  for these samples is due to presence of lesser amount of residual carbon. Moreover, the  $C_{dl}$  value of PT6 as estimated is 12.2 mFcm<sup>-2</sup>. The results predict that the incorporation of Mo<sub>2</sub>C in the graphitic carbon residue enhances the charge storage capacity. The  $C_{dl}$  measurements reveal that high temperature synthesized Mo<sub>2</sub>C nanostructures encapsulated in conductive carbon layers obtained from waste plastics during in-situ synthesis are novel materials for energy storage applications. The  $C_{dl}$  measurements also predict the largest electrochemical surface area (ECSA) of Mo<sub>2</sub>C particles in PT3 as compared to PT6 (Figs. S14 and S1) embedded in graphitic carbon matrix contributes to their HER activity (Zhang et al., 2015). The TEM & FESEM micrographs of PT3 showing faceted stacking makes the exterior sheet surface available for electrolyte ions, which improves the  $C_{dl}$  value. The variation of specific capacitance corresponding to multiple scan rates is shown in (Fig. 6d). The specific capacitance of PT6 is 162.5 Fg<sup>-1</sup> at 50 mVs<sup>-1</sup> and 44.5 Fg<sup>-1</sup> at 320 mVs<sup>-1</sup>. However, the specific capacitance of PT3 is 55.6 Fg<sup>-1</sup> at 50 mVs<sup>-1</sup> and 37.3 Fg<sup>-1</sup> at 320 mVs<sup>-1</sup>. The retention of capacitance

at higher scan rates as shown in (Fig. 6d) is enhanced by higher amount of surface carbon having thicker graphitic carbon coating over Mo<sub>2</sub>C. The results predict the loss of specific capacitance in PT6 and PT3 by ~73 and 33%, respectively at 320 mVs<sup>-1</sup>. The enhanced charge storage capacity apart from BET surface area may be attributed to variation in pore size, shape and surface functionalization. The meso and micro pores inter connected in the supported carbon nanostructures improve the charge transfer, accommodation and distribution, which utilize all the surface of the electrode material. The HER performance of PT1 although having low  $C_{dl}$  value is due to lower particle size and higher specific surface area.

### 3.7.3. Electrochemical impedance spectroscopy (EIS)

EIS measurements were done at different potential to gather more insight into the electrocatalytic activity of synthesized nano powders. The information regarding the adsorption/desorption and reaction kinetics on the catalyst surface can be revealed. The EIS of the synthesized samples are shown by the Nyquist plots as represented in (Fig. S15 a-f, SI). The charge transfer resistance decreases with increase in the potential as can be seen from the EIS curve nearly forming semicircular curve of decreased radius. Among all the synthesized samples, only PT2, PT3 and PT6 tend to form the nearly semicircular curves at higher potential values. The deviation from the perfectly semicircular curve of Nyquist corresponds to the presence of constant phase element (CPE) and attributes to hydrogen ion adsorption on catalyst surface. This could be the result of inhomogeneous surface characteristics developed during in-situ synthesis. The results reveal the increase in charge kinetics

with the increment in surface graphitic carbon layer over Mo<sub>2</sub>C. The electronic bridge of graphitic carbon deposited over and inter-connecting the Mo<sub>2</sub>C particles enhances electrical conductivity and improves the electron transfer kinetics corresponding to HER process.

#### 4. Conclusion

The present study reports the utilization of waste plastics to get the useful product MoC at 600 °C and Mo<sub>2</sub>C at 700–800 °C for energy conversion and storage applications. The synthesized product MoC shows enhanced current density 34 mAcm<sup>-2</sup> at lower potential value due to higher surface area. The pure phase Mo<sub>2</sub>C embedded in graphitic carbon matrix exhibits smaller Tafel slope values of 93.9, 82.6 and 80.11 mVdec<sup>-1</sup> for PT2, PT3 and PT6, respectively. The faceted stacking of graphitic layers enclosing the Mo<sub>2</sub>C particles (PT3) makes the exterior surface of sheet available for electrolyte ions and improves the storage capacity and reaction kinetics. The thickness of graphitic carbon layer influences the capacitance retention at multiple scan rates. The present study provides a way to use the plastic wastes for the synthesis of carbonaceous materials for energy production and capacitor applications. The environmental issues caused due to plastic wastes is addressed properly.

#### Conflicts of interest

No conflicts.

#### Acknowledgement

The Authors are highly thankful to Dr. Anup Thakur, Assistant professor Punjabi University, Patiala for carrying out the Rietveld refinement. The authors also offer special gratitude to SAI Lab, TIET for XRD and SAIF, Punjab University, Chandigarh for FESEM analysis. Authors express special thanks to AIRF, JNU, NewDelhi for TEM and HRTEM analysis. The authors are thankful to Dr. B. N. Chudasama and Dr. SoumenBasu for TGA and N<sub>2</sub> adsorption-desorption characterizations. One of the authors R. A. M is thankful TIET, Patiala for financial support. The offer special thanks to UGC-DAE Consortium for Scientific Research for carrying out the work under the project (CSR-IC-239/2017-18/1320).

#### Appendix A. Supplementary data

Supplementary data to this article can be found online at <https://doi.org/10.1016/j.jclepro.2019.02.004>.

#### References

- Alhajri, N.S., Anjum, D.H., Takanabe, K., 2014. Molybdenum carbide-carbon nanocomposites synthesized from a reactive template for electrochemical hydrogen evolution. *J. Mater. Chem. A* 2, 10548. <https://doi.org/10.1039/c4ta00577e>.
- Anuar Sharuddin, S.D., Abnisa, F., Wan Daud, W.M.A., Aroua, M.K., 2016. A review on pyrolysis of plastic wastes. *Energy Convers. Manag.* 115, 308–326. <https://doi.org/10.1016/j.enconman.2016.02.037>.
- Barbarias, I., Lopez, G., Artetxe, M., Arregi, A., Bilbao, J., Olazar, M., 2018. Valorisation of different waste plastics by pyrolysis and in-line catalytic steam reforming for hydrogen production. *Energy Convers. Manag.* 156, 575–584. <https://doi.org/10.1016/j.enconman.2017.11.048>.
- Begum, S., Rasul, M.G., Akbar, D., 2012. An investigation on thermo chemical conversions of solid waste for energy recovery. *Int. J. Environ. Ecol. Eng.* 6, 624–630.
- Brar, L.K., Singla, G., Pandey, O.P., 2016. The role of carbon in structural evolution during single step synthesis of nano tantalum carbide. *RSC Adv.* 6, 109174–109184. <https://doi.org/10.1039/C6RA24484J>.
- Chen, Y., Zhang, H., Zhang, J., Ma, J., Ye, H., Qian, G., Ye, Y., Zhong, S., 2011. Facile synthesis and thermal stability of nanocrystalline molybdenum carbide. *Mater. Sci. Appl.* 02, 1313–1316. <https://doi.org/10.4236/msa.2011.29178>.
- Chen, Z., Lv, C., Chen, Z., Jin, L., Wang, J., Huang, Z., 2014. Molybdenum phosphide flakes catalyze hydrogen generation in acidic and basic solutions. *Am. J. Anal. Chem.* 5, 1200–1213.
- Choi, J.-S., Bugli, G., Ega-Mariadassou, D., 2000. Influence of the degree of carburization on the density of sites and hydrogenating activity of molybdenum carbides. *J. Catal.* 193, 238–247. <https://doi.org/10.1006/jcat.2000.2894>.
- Christensen, E., 2016. Transition Metal Carbides ( WC , Mo<sub>2</sub>C , TaC , NbC ) as Potential Electrocatalysts for the Hydrogen Evolution Reaction ( HER ) at Medium Temperatures ScienceDirect. <https://doi.org/10.1016/j.ijhydene.2014.12.076>.
- Daio, T., Staykov, A., Guo, L., Liu, J., Tanaka, M., Matthew Lyth, S., Sasaki, K., 2015. Lattice strain mapping of platinum nanoparticles on carbon and SnO<sub>2</sub> supports. *Sci. Rep.* 5, 13126. <https://doi.org/10.1038/srep13126>.
- Dang, J., Zhang, G., Wang, L., Chou, K., Pistorius, P.C., 2015. Study on Reduction of MoO<sub>2</sub> Powders with CO to Produce Mo<sub>2</sub>C 6, 1–6. <https://doi.org/10.1111/jace.14042>.
- Das, A., Chakraborty, B., Sood, A.K., 2008. Raman spectroscopy of graphene on different substrates and influence of defects. *Bull. Mater. Sci.* 31, 579–584. <https://doi.org/10.1007/s12034-008-0090-5>.
- Ding, R., Wu, Y., Chen, Y., Chen, H., Wang, J., Shi, Y., Yang, M., 2016. Catalytic hydrodeoxygenation of palmitic acid over a bifunctional Co-doped MoO<sub>2</sub>/CNTs catalyst: an insight into the promoting effect of cobalt. *Catal. Sci. Technol.* 6, 2065–2076. <https://doi.org/10.1039/C5CY01575H>.
- El, B.Y., Parth, W.I.N., 1963. The Structure of Dimolybdenum Carbide by Neutron Diffraction Technique\* 2, pp. 202–205. <https://doi.org/10.1107/S0365110X63000487>.
- Ferrari, A.C., 2007. Raman spectroscopy of graphene and graphite: disorder, electron-phonon coupling, doping and nonadiabatic effects. *Solid State Commun.* 143, 47–57. <https://doi.org/10.1016/j.ssc.2007.03.052>.
- Ferrari, A.C., Robertson, J., 2000. Interpretation of Raman spectra of disordered and amorphous carbon. *Phys. Rev. B* 61, 14–295.
- Gao, Q., Zhao, X., Xiao, Y., Zhao, D., Cao, M., 2014. A mild route to mesoporous Mo<sub>2</sub>C-C hybrid nanospheres for high performance lithium-ion batteries. *Nanoscale* 6, 6151–6157. <https://doi.org/10.1039/c3nr06678a>.
- Hazrat, M.A., Rasul, M.G., Khan, M.M.K., Azad, A.K., Bhuiya, M.M.K., 2014. Utilization of polymer wastes as transport fuel resource as recent development. *Energy Procedia* 61, 1681–1685. <https://doi.org/10.1016/j.egypro.2014.12.191>.
- Hu, K.H., Hu, X.G., Sun, X.J., 2010. Morphological effect of MoS<sub>2</sub> nanoparticles on catalytic oxidation and vacuum lubrication. *Appl. Surf. Sci.* 256, 2517–2523. <https://doi.org/10.1016/j.apsusc.2009.10.098>.
- Huang, Y., Gong, Q., Song, X., Feng, K., Nie, K., Zhao, F., Wang, Y., Zeng, M., Zhong, J., Li, Y., 2016. Mo<sub>2</sub>C nanoparticles dispersed on hierarchical carbon microflowers for efficient electrocatalytic hydrogen evolution. *ACS Nano* 10, 11337–11343. <https://doi.org/10.1021/acs.nano.6b06580>.
- Krasnenko, V., Brik, M.G., 2012. First-principles calculations of hydrostatic pressure effects on the structural , elastic and thermodynamic properties of cubic monocarbides X C ( X % Ti , V , Cr , Nb , Mo , Hf ). *Solid State Sci.* 14, 1431–1444. <https://doi.org/10.1016/j.solidstatesciences.2012.08.007>.
- Lad, K.N., Pratap, A., 2006. Crystallite size estimation of elemental and composite silver nano-powders using XRD principles. *Indian J. Pure Appl. Phys.* 44, 157–161.
- Lee, Y.J., Kim, S.H., Lee, T.H., Nersisyan, H.H., Lee, K.H., Han, M.H., Jeong, S.U., Kang, K.S., Bae, K.K., Lee, J.H., 2014. Combustion synthesis and characterization of TaC, TaC/TaSi<sub>2</sub>, and TaC/TaB nanoparticles. *Chem. Eng. Sci.* 107, 227–234. <https://doi.org/10.1016/j.ces.2013.12.015>.
- Leis, J., Perkson, A., 2010. The Effect of Mo<sub>2</sub>C Derived Carbon Pore Size on the Electrical Double-Layer Characteristics in Propylene Carbonate-Based Electrolyte 8, pp. 1–8. <https://doi.org/10.1016/j.carbon.2010.07.003>.
- Levy, R.B., Boudart, M., 1973. Platinum-like behavior of tungsten carbide in surface catalysis. *Science* (80- ) 181, 547–549.
- Li, J.-S., Wang, Y., Liu, C.-H., Li, S.-L., Wang, Y.-G., Dong, L.-Z., Dai, Z.-H., Li, Y.-F., Lan, Y.-Q., 2016. Coupled molybdenum carbide and reduced graphene oxide electrocatalysts for efficient hydrogen evolution. *Nat. Commun.* 7, 11204. <https://doi.org/10.1038/ncomms11204>.
- Liao, L., Wang, S., Xiao, J., Bian, X., Zhang, Y., 2014. A nanoporous molybdenum carbide nanowire as an electrocatalyst for hydrogen evolution reaction †. *Energy Environ. Sci.* 7, 387–392. <https://doi.org/10.1039/c3ee42441c>.
- Liu, Y., Zhu, M., Chen, D., 2015. Sheet-like MoS<sub>2</sub>/C composites with enhanced Li-ion storage properties. *J. Mater. Chem. A* 3, 11857–11862. <https://doi.org/10.1039/C5TA02100F>.
- Lopez, G., Artetxe, M., Amutio, M., Alvarez, J., Bilbao, J., Olazar, M., 2018. Recent advances in the gasification of waste plastics. A critical overview. *Renew. Sustain. Energy Rev.* 82, 576–596. <https://doi.org/10.1016/j.rser.2017.09.032>.
- Ma, D., Lu, Z., Tang, Y., Li, T., Tang, Z., Yang, Z., 2014. Effect of lattice strain on the oxygen vacancy formation and hydrogen adsorption at CeO<sub>2</sub>(111) surface. *Phys. Lett. A* 378, 2570–2575. <https://doi.org/10.1016/j.physleta.2014.07.006>.
- McKone, J.R., Marinescu, S.C., Brunschwig, B.S., Winkler, J.R., Gray, H.B., 2014. Earth-abundant hydrogen evolution electrocatalysts. *Chem. Sci.* 5, 865–878. <https://doi.org/10.1039/C3SC51711J>.
- Michalsky, R., Zhang, Y.J., Peterson, A.A., 2014. Trends in the hydrogen evolution activity of metal carbide catalysts. *ACS Catal.* 4, 1274–1278. <https://doi.org/10.1021/cs500056u>.
- Mir, R.A., Pandey, O.P., 2018. Influence of graphitic/amorphous coated carbon on HER activity of low temperature synthesized β-Mo<sub>2</sub>C/C nanocomposites. *Chem. Eng. J.* 348, 1037–1048. <https://doi.org/10.1016/j.cej.2018.05.041>.
- Mir, R.A., Sharma, P., Pandey, O.P., 2017. Thermal and structural studies of carbon



- coated Mo<sub>2</sub>C synthesized via in-situ single step reduction-carburization. *Sci. Rep.* 7, 3518. <https://doi.org/10.1038/s41598-017-03197-8>.
- Miskolczi, N., Angyal, A., Bartha, L., Valkai, I., 2009. Fuels by pyrolysis of waste plastics from agricultural and packaging sectors in a pilot scale reactor. *Fuel Process. Technol.* 90, 1032–1040. In: <https://doi.org/10.1016/j.fuproc.2009.04.019>.
- Mo, T., Xu, J., Yang, Y., Li, Y., 2015. Effect of carburization protocols on molybdenum carbide synthesis and study on its performance in CO hydrogenation. *Catal. Today* 1–15. <https://doi.org/10.1016/j.cattod.2015.07.014>.
- Mu, Y., Zhang, Y., Fang, L., Liu, L., Zhang, H., Wang, Y., 2016. Controllable synthesis of molybdenum carbide nanoparticles embedded in porous graphitized carbon matrices as efficient electrocatalyst for hydrogen evolution reaction. *Electrochim. Acta* 215, 357–365. <https://doi.org/10.1016/j.electacta.2016.08.104>.
- Ohnishi, S., Fujii, M., Ohata, M., Rokuta, I., Fujita, T., 2018. Efficient energy recovery through a combination of waste-to-energy systems for a low-carbon city. *Resour. Conserv. Recycl.* 128, 394–405. <https://doi.org/10.1016/j.resconrec.2016.11.018>.
- Ojha, K., Saha, S., Banerjee, S., Ganguli, A.K., 2017. Efficient electrocatalytic hydrogen evolution from MoS<sub>2</sub>-functionalized Mo<sub>2</sub>N nanostructures. *ACS Appl. Mater. Interfaces* 9, 19455–19461. <https://doi.org/10.1021/acsami.6b10717>.
- Pang, M., Li, C., Ding, L., Zhang, J., Su, D., Li, W., Liang, C., 2010. Microwave-assisted preparation of Mo<sub>2</sub>C/CNTs nanocomposites as efficient electrocatalyst supports for oxygen reduction reaction. *Ind. Eng. Chem. Res.* 49, 4169–4174. <https://doi.org/10.1021/ie901741c>.
- Qiao, S.Z., Zheng, Y., Jiao, Y., Jaroniec, M., Qiao, S.Z., 2015. Advancing the electrochemistry of the hydrogen evolution reaction through combining experiment and theory. *Angew. Minireviews* 54, 52–65. <https://doi.org/10.1002/anie.201407031>.
- Ramos, A., Monteiro, E., Silva, V., Rouboa, A., 2018. Co-gasification and recent developments on waste-to-energy conversion: a review. *Renew. Sustain. Energy Rev.* 81, 380–398. <https://doi.org/10.1016/j.rser.2017.07.025>.
- Rather, R.A., Singh, S., Pal, B., 2017a. A Cu<sup>+</sup>/Cu<sup>0</sup>-TiO<sub>2</sub> mesoporous nanocomposite exhibits improved H<sub>2</sub> production from H<sub>2</sub>O under direct solar irradiation. *J. Catal.* 346, 1–9. <https://doi.org/10.1016/j.jcat.2016.11.021>.
- Rather, R.A., Singh, S., Pal, B., 2017b. A C<sub>3</sub>N<sub>4</sub> surface passivated highly photoactive Au-TiO<sub>2</sub> tubular nanostructure for the efficient H<sub>2</sub> production from water under sunlight irradiation. *Appl. Catal. B Environ.* 213, 9–17. <https://doi.org/10.1016/j.apcatb.2017.05.002>.
- Shi, Z., Wang, Y., Lin, H., Zhang, H., Shen, M., Xie, S., Zhang, Y., Gao, Q., Tang, Y., 2016. Porous nanoMoC@graphite shell derived from a MOFs-directed strategy: an efficient electrocatalyst for the hydrogen evolution reaction. *J. Mater. Chem. A* 4, 6006–6013. <https://doi.org/10.1039/C6TA01900E>.
- Shi, Z., Nie, K., Shao, Z.-J., Gao, B., Lin, H., Zhang, H., Liu, B., Wang, Y., Zhang, Y., Sun, X., Cao, X.-M., Hu, P., Gao, Q., Tang, Y., 2017. Phosphorus-Mo<sub>2</sub>C@carbon nanowires toward efficient electrochemical hydrogen evolution: composition, structural and electronic regulation. *Energy Environ. Sci.* 10, 1262–1271. <https://doi.org/10.1039/C7EE00388A>.
- Sljukic, B., Vujkovic, M., Amaral, L., Santos, D.M.F., Rocha, R.P., Sequeira, C.A.C., Figueiredo, J.L., 2015. Carbon-supported Mo<sub>2</sub>C electrocatalysts for hydrogen evolution reaction. *J. Mater. Chem. A* 3, 15505–15512. <https://doi.org/10.1039/C5TA02346G>.
- Sun, W., Wang, Z., Zaman, W.Q., Zhou, Z., Cao, L., Gong, X.-Q., Yang, J., 2018. Effect of lattice strain on the electro-catalytic activity of IrO<sub>2</sub> for water splitting. *Chem. Commun.* 54, 996–999. <https://doi.org/10.1039/C7CC09580E>.
- Tang, C., Wu, Z., Wang, D., 2016. Influence of carbon on molybdenum carbide catalysts for the hydrogen evolution reaction. *ChemCatChem* 8, 1961–1967. <https://doi.org/10.1002/cctc.201600107>.
- Tomas-Garcia, A.L., Li, Q., Jensen, J.O., Bjerrum, N.J., 2014. High surface area tungsten carbides: synthesis, characterization and catalytic activity towards the hydrogen evolution reaction in phosphoric acid at elevated temperatures. *Int. J. Electrochem. Sci.* 9, 1016–1032.
- Vrubel, H., Hu, X., 2012. Molybdenum boride and carbide catalyze hydrogen evolution in both acidic and basic solutions. *Angew. Chem. Int. Ed.* 51, 12703–12706. <https://doi.org/10.1002/anie.201207111>.
- Wan, C., Regmi, Y.N., Leonard, B.M., 2014. Multiple phases of molybdenum carbide as electrocatalysts for the hydrogen evolution reaction. *Angew. Chem. Int. Ed.* 53, 6407–6410. <https://doi.org/10.1002/anie.201402998>.
- Wang, B., Wang, G., Wang, H., 2015. Hybrids of Mo<sub>2</sub>C nanoparticles anchored on graphene sheets as anode materials for high performance lithium-ion batteries. *J. Mater. Chem. A* 3, 17403–17411. <https://doi.org/10.1039/C5TA03929K>.
- Wu, H., Wang, X., Bai, Y., Jiang, L., Wu, C., Hu, B., Wei, Q., Liu, X., Li, N., 2013. The effects of preparation temperature on microstructure and electrochemical performance of calcium carbide-derived carbon. *J. Solid State Electrochem.* 17, 2453–2460. <https://doi.org/10.1007/s10008-013-2126-z>.
- Wu, H., Bin, Xia, B.Y., Yu, L., Yu, X.Y., Lou, X.W., 2015. Porous molybdenum carbide nano-octahedrons synthesized via confined carburization in metal-organic frameworks for efficient hydrogen production. *Nat. Commun.* 6, 1–17. <https://doi.org/10.1038/ncomms7512>.
- Xiao, P., Yan, Y., Ge, X., Liu, Z., Wang, J.Y., Wang, X., 2014. Investigation of molybdenum carbide nano-rod as an efficient and durable electrocatalyst for hydrogen evolution in acidic and alkaline media. *Appl. Catal. B Environ.* 154–155, 232–237. <https://doi.org/10.1016/j.apcatb.2014.02.020>.
- Xiao, P., Ge, X., Wang, H., Liu, Z., Fisher, A., Wang, X., 2015. Novel Molybdenum Carbide – Tungsten Carbide Composite Nanowires and Their Electrochemical Activation for Efficient and Stable Hydrogen Evolution, pp. 1520–1526. <https://doi.org/10.1002/adfm.201403633>.
- Yang, X.J., Feng, X.J., Tan, H.Q., Zang, H.Y., Wang, X.L., Wang, Y.H., Wang, E.B., Li, Y.G., 2016. N-Doped graphene-coated molybdenum carbide nanoparticles as highly efficient electrocatalysts for the hydrogen evolution reaction. *J. Mater. Chem. A* 4, 3947–3954. <https://doi.org/10.1039/c5ta09507g>.
- Yao, D., Zhang, Y., Williams, P.T., Yang, H., Chen, H., 2018. Co-production of hydrogen and carbon nanotubes from real-world waste plastics: influence of catalyst composition and operational parameters. *Appl. Catal. B Environ.* 221, 584–597. <https://doi.org/10.1016/j.apcatb.2017.09.035>.
- Youn, D.H., Han, S., Kim, J.Y., Kim, J.Y., Park, H., Choi, S.H., Lee, J.S., 2014. Highly active and stable hydrogen evolution electrocatalysts based on molybdenum compounds on carbon nanotube-graphene hybrid support. *ACS Nano* 8, 5164–5173. <https://doi.org/10.1021/nn5012144>.
- Zhang, K., Li, C., Zhao, Y., Yu, X., Chen, Y., 2015. Porous one-dimensional Mo<sub>2</sub>C-amorphous carbon composites: high-efficient and durable electrocatalysts for hydrogen generation. *Phys. Chem. Chem. Phys.* 17, 16609–16614. <https://doi.org/10.1039/C5CP02028J>.
- Zhang, Y., Nahil, M.A., Wu, C., Williams, P.T., 2017. Pyrolysis-catalysis of waste plastic using a nickel-stainless-steel mesh catalyst for high-value carbon products. *Environ. Technol.* 38, 2889–2897. <https://doi.org/10.1080/09593330.2017.1281351>.
- Zhao, Y., Yao, Z., Shi, Y., Qiao, X., Wang, G., Wang, H., Yin, J., Peng, F., 2015. A novel approach to the synthesis of bulk and supported b-Mo<sub>2</sub>C using dimethyl ether as a carbon source. *New J. Chem.* 39, 4901–4908. <https://doi.org/10.1039/c5nj00395d>.
- Zhong, Y., Xia, X., Shi, F., Zhan, J., Tu, J., Fan, H.J., 2016. Transition metal carbides and nitrides in energy storage and conversion. *Adv. Sci.* 3, 1500286. <https://doi.org/10.1002/advs.201500286>.
- Zou, X., Zhang, Y., 2015. Noble metal-free hydrogen evolution catalysts for water splitting. *Chem. Soc. Rev.* 44, 5148–5180. <https://doi.org/10.1039/C4CS00448E>.